

This article was downloaded by: [Universiteit Twente]

On: 14 May 2014, At: 05:23

Publisher: Taylor & Francis

Informa Ltd Registered in England and Wales Registered Number: 1072954 Registered office: Mortimer House, 37-41 Mortimer Street, London W1T 3JH, UK



Computer Methods in Biomechanics and Biomedical Engineering

Publication details, including instructions for authors and subscription information:

<http://www.tandfonline.com/loi/gcmb20>

On the importance of modelling organ geometry and boundary conditions for predicting three-dimensional prostate deformation

Alex Jahya^a, Martijn G. Schouten^b, Jurgen J. Fütterer^b & Sarthak Misra^a

^a MIRA - Institute for Biomedical Technology and Technical Medicine, University of Twente, Enschede, The Netherlands

^b Department of Radiology, Radboud University Nijmegen Medical Centre, Nijmegen, The Netherlands

Published online: 06 Jul 2012.

To cite this article: Alex Jahya, Martijn G. Schouten, Jurgen J. Fütterer & Sarthak Misra (2014) On the importance of modelling organ geometry and boundary conditions for predicting three-dimensional prostate deformation, Computer Methods in Biomechanics and Biomedical Engineering, 17:5, 497-506, DOI: [10.1080/10255842.2012.694876](https://doi.org/10.1080/10255842.2012.694876)

To link to this article: <http://dx.doi.org/10.1080/10255842.2012.694876>

PLEASE SCROLL DOWN FOR ARTICLE

Taylor & Francis makes every effort to ensure the accuracy of all the information (the "Content") contained in the publications on our platform. However, Taylor & Francis, our agents, and our licensors make no representations or warranties whatsoever as to the accuracy, completeness, or suitability for any purpose of the Content. Any opinions and views expressed in this publication are the opinions and views of the authors, and are not the views of or endorsed by Taylor & Francis. The accuracy of the Content should not be relied upon and should be independently verified with primary sources of information. Taylor and Francis shall not be liable for any losses, actions, claims, proceedings, demands, costs, expenses, damages, and other liabilities whatsoever or howsoever caused arising directly or indirectly in connection with, in relation to or arising out of the use of the Content.

This article may be used for research, teaching, and private study purposes. Any substantial or systematic reproduction, redistribution, reselling, loan, sub-licensing, systematic supply, or distribution in any form to anyone is expressly forbidden. Terms & Conditions of access and use can be found at <http://www.tandfonline.com/page/terms-and-conditions>

On the importance of modelling organ geometry and boundary conditions for predicting three-dimensional prostate deformation

Alex Jahya^{a*}, Martijn G. Schouten^b, Jurgen J. Fütterer^b and Sarthak Misra^a

^aMIRA – Institute for Biomedical Technology and Technical Medicine, University of Twente, Enschede, The Netherlands;

^bDepartment of Radiology, Radboud University Nijmegen Medical Centre, Nijmegen, The Netherlands

(Received 24 January 2012; final version received 15 May 2012)

The use of an ultrasound probe or a needle guide during biopsy deforms both the rectal wall and the prostate, resulting in lesion motion. An accurate patient-specific finite element (FE)-based biomechanical model can be used to predict prostate deformations. In this study, an FE model of a prostate phantom is developed using magnetic resonance images, while soft-tissue elasticity is estimated *in vivo* using an ultrasound-based acoustic radiation force impulse imaging technique. This study confirms that three-dimensional FE-predicted prostate deformation is predominantly dependent on accurate modelling of prostate geometry and boundary conditions. Upon application of various compressive displacements, our results show that a linear elastic FE model can accurately predict prostate deformations. The maximum global error between FE-predicted simulations and experimental results is 0.76 mm. Moreover, the effect of including the urethra, puboprostatic ligament and urinary bladder on prostate deformations is investigated by a sensitivity study.

Keywords: biopsy; computer-assisted surgical simulation; finite element modelling; magnetic resonance; needle insertion; ultrasound

1. Introduction

Biopsy is the most commonly performed minimally invasive surgical procedure for the diagnosis of prostate cancer. During the procedure, a needle is inserted into the prostate and tissue samples are obtained from the region of interest (Shahrokh and Claus 2008). The suspected lesion location is determined prior to the procedure using diagnostic medical images (Karnik et al. 2010). For an accurate diagnosis, the needle tip has to be placed within a spherical radius of 2.5 mm from the suspected lesion.

Since size of the prostate is relatively small (approximately 40 mm × 20 mm × 20 mm), accurate needle tip positioning during the procedure is crucial (Benninghoff 1993). Misplacement of the needle tip often leads to surgical complications such as tissue trauma or urinary incontinence (Wust et al. 2004). During the intervention, physicians routinely use transrectal ultrasound (TRUS) or magnetic resonance (MR) images as guidance to accurately target the suspected lesion (Anastasiadis et al. 2006; Hu et al. 2008).

However, the use of an ultrasound probe during TRUS biopsy or a needle guide during MR-guided biopsy deforms both the rectal wall and the prostate, resulting in motion of the suspected lesion (Figure 1). This can lead to misdiagnosis since the intended biopsy region is based on diagnostic images of the prostate in the undeformed shape. An accurate patient-specific biomechanical model can aid

physicians by predicting prostate deformations prior to the procedure. This will reduce needle-targeting error, leading to a more conclusive diagnosis.

A biomechanical model based on finite element (FE) analysis is one of the methods proposed for predicting prostate deformations (Misra et al. 2008). A complex FE model can be developed using current medical imaging modalities such as computed tomography (CT) or MR images. These imaging modalities provide a clear visualisation of prostate geometry and surrounding structures that support it. Previous work has shown the potential of using an FE model for the non-real-time predictions of soft-tissue deformations (Mohamed et al. 2002; Alterovitz et al. 2006; Crouch et al. 2007; Misra et al. 2009). However, the use of an accurate three-dimensional (3D) FE-based biomechanical model for surgical pre-operative planning is yet to be fully explored and still remains a challenge.

One of the hurdles in developing an accurate biomechanical model is to incorporate soft-tissue properties. Soft tissue is anisotropic, inhomogeneous, viscoelastic and exhibits nonlinear elastic behaviour. Furthermore, soft-tissue properties vary significantly between *in vivo* and *ex vivo* measurements (Ottensmeyer et al. 2007). Moreover, in order to use an FE analysis to accurately predict prostate deformations, changes in prostate geometry, boundary and loading conditions have to be accounted for. Prostate geometry and boundary conditions could

*Corresponding author. Email: a.jahya@utwente.nl

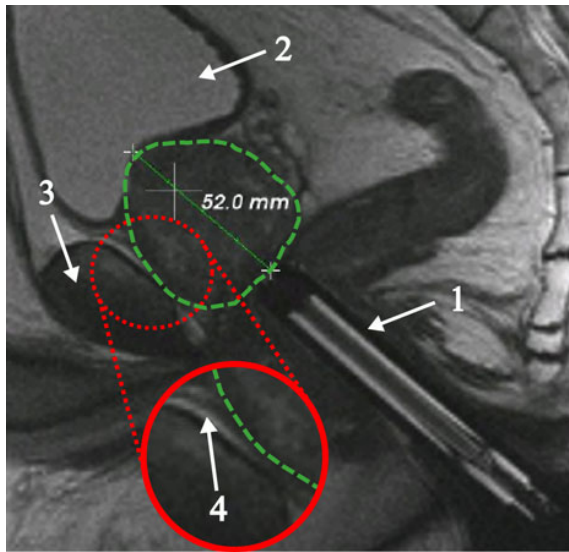


Figure 1. MR image of a deformed prostate due to applied displacement of the needle guide. (1) Needle guide, (2) urinary bladder, (3) pubic bone and (4) puboprostatic ligament (inset). The urethra, seminal vesicle and penis are not visible in the MR image above. The longest length of the undeformed prostate is 58.9 mm. The deformed-prostate outline is shown by a green dashed-line.

change due to patient motion, or physiological processes such as bladder filling and breathing. On the other hand, loading conditions could vary due to changes in applied displacements of the ultrasound probe or needle guide, which is used during the procedure.

Previous work by Ophir et al. (1991) and Goertz et al. (2010) showed that it is possible to estimate linear elastic soft-tissue properties *in vivo* and non-invasively for small strain using ultrasound-based tools such as elastography and acoustic radiation force impulse (ARFI) imaging technique, respectively. Davatzikos et al. (2001) presented that variations in boundary conditions and elastic material properties affect prostate deformations. Furthermore, Misra et al. (2009) presented that geometry and boundary conditions dominate soft-tissue deformation response, rather than its properties. This hypothesis was further validated by Op den Buijs et al. (2011). They demonstrated that by using an FE-based approach, elastography and known boundary conditions, it is possible to accurately predict the two-dimensional (2D) displacements of a lesion upon compression and indentation of a breast-shaped phantom.

In our study, we extend the results earlier shown by Misra et al. (2009) in 2D to the analysis of 3D prostate deformations. The goal of our study was to confirm that 3D prostate deformation is also predominantly dependent on accurate modelling of anatomical details (prostate geometry and boundary conditions). Hence, a linear

elastic FE model can be used to accurately predict prostate deformations. In our study, FE simulation results are validated with MR experimental results. The validated FE model is then used to predict prostate deformations under various applied displacements and boundary conditions.

Furthermore, we also investigate the effect of increasing fidelity (in terms of organs and structures surrounding the prostate) of the FE model. Organs and structures included are the urethra, puboprostatic ligament and urinary bladder. These organs and structures are chosen because of their vicinities to the prostate; hence, the possibility that they might influence prostate deformations during the surgical intervention. In the human anatomy, the prostate is situated directly below the urinary bladder, and completely surrounds the urethra – a channel that runs from the urinary bladder to the penis (Figure 1 – the urethra and penis are not shown in the figure). Physiological bladder filling during the procedure changes size of the urinary bladder (Nichol et al. 2007). Moreover, the prostate is attached to the pubic bone by the puboprostatic ligament. The anatomical details of the organs and structures surrounding the prostate might vary from one patient to another.

The novel aspect of our study is to show that by accurately modelling anatomical details in 3D, a linear elastic FE model can predict prostate deformations. Furthermore, the results of our study also show that a combination of well-established medical imaging modalities (ultrasound and MR images) and FE analysis can be used to develop an accurate 3D patient-specific biomechanical model. Such a model could be used for pre-operative planning in order to reduce needle-targeting error during the procedure.

2. Materials and methods

First, in Section 2.1, details of the experimental set-up conducted in an MR imaging system are presented. Furthermore, the experimental cases and sensitivity study scenarios are also described in this section. Second, in Section 2.2, the theory of a linear elastic constitutive model is briefly described. Finally, in Section 2.3, the contact boundary conditions that are used in the FE model are described.

2.1 Experimental set-up and sensitivity study

Experiments are performed using an MR-compatible prostate phantom (Model 053, Computerized Imaging Reference Systems, Inc., Norfolk, VA, USA), a Dynatrim needle guide positioner and a needle guide (Invivo, Gainesville, FL, USA) (Figure 2(a)–(c)). A closed-bore 3T MR imaging system (Magnetom Skyra, Siemens Medical Solutions, Erlangen, Germany) is used for the

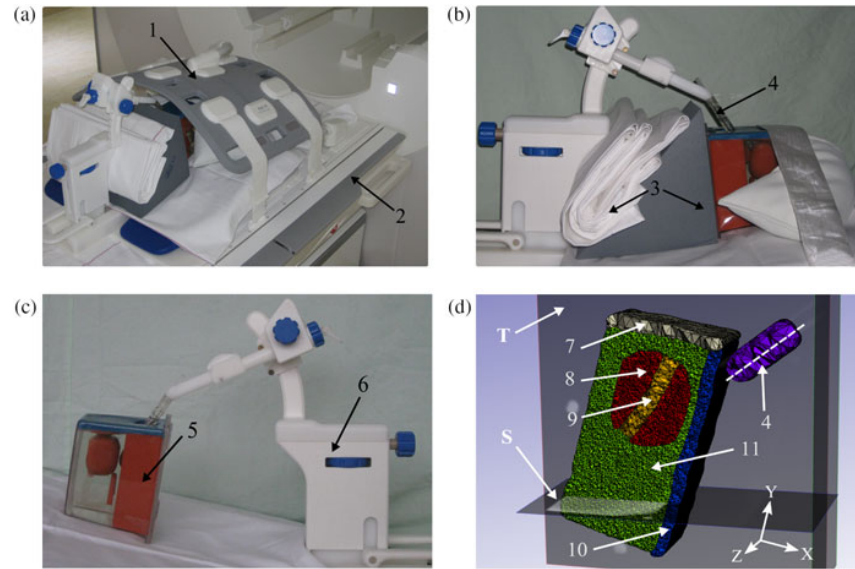


Figure 2. (a)–(c) Experimental set-up conducted in a MR imaging system and (d) FE model of the prostate phantom with transverse (T) and sagittal (S) planes. Prostate phantom is shown in xy -plane mesh view. For clarity, supports, cushion, etc. have been removed in (c). Moreover, in (d), the needle guide cylindrical axis and axis convention are also presented. The cylindrical axis is shown with a white dashed-line. Furthermore, the urethra passes through the prostate. (1) Body coil, (2) table, (3) supports, (4) needle guide, (5) prostate phantom, (6) needle guide positioner, (7) perineal membrane, (8) prostate, (9) urethra, (10) rectal wall and (11) surrounding gel.

experiments. Furthermore, a body-array coil is also used to increase MR signal reception (item #1, Figure 2(a)). The prostate phantom is enclosed within a $115 \times 70 \times 95 \text{ mm}^3$ clear acrylic container, and contains structures that model the prostate, rectal wall and urethra (Figure 2(d)).

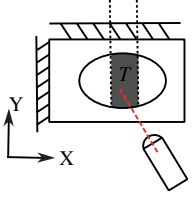
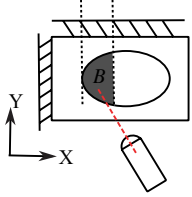
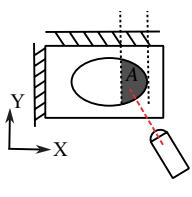
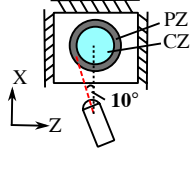
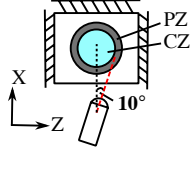
During the experiments, the needle guide positioner (item #6, Figure 2(c)) is mounted on the table of the MR imaging system (item #2, Figure 2(a)). Subsequently, the prostate phantom (item #5, Figure 2(c)) is secured tightly by the supports (item #3, Figure 2(b)) and cushion, and strapped to the table. This ensures that the prostate phantom does not move during the experiments. The needle guide positioner (item #6, Figure 2(c)), which is fixed to the table, also provides a fixed support. The needle guide (item #4, Figure 2(b),(d)) is then placed inside the rectal cavity of the prostate phantom with the tip of the guide touching the rectal wall (item #10, Figure 2(d)). The needle guide is positioned such that it is located at the centre of the rectal cavity, and its cylindrical axis is oriented towards the direction of the prostate (item #8, Figure 2(d)).

Subsequently, the prostate phantom is deformed using the needle guide for 9 and 18 mm applied displacements along the guide cylindrical axis. MR imaging is done with the following settings: repetition time = 4.6 ms, echo time = 2.3 ms, flip angle = 43° and resolution = $1.0 \text{ mm} \times 1.0 \text{ mm} \times 1.0 \text{ mm}$. 3D MR images of the prostate are acquired in the undeformed, and 9 and 18 mm applied displacement states for the following five experimental cases (Table 1):

- (1) *Transition (T)*: Compressive displacements of 9 and 18 mm are applied to the transition zone of the prostate. The transition zone of the prostate is defined for the centre part of the prostate that surrounds the urethra (Kundra et al. 2007).
- (2) *Base (B)*: Identical applied displacements as for *T*; however, displacements are applied to the base of the prostate. The base of the prostate is defined for a wide part at the top of the prostate, which is contiguous with the urinary bladder wall.
- (3) *Apex (A)*: Identical applied displacements as for *T*; however, displacements are applied to the apex of the prostate. The apex of the prostate is defined for the tip of the prostate, i.e. the part of the prostate that is the farthest away from the urinary bladder.
- (4) *Transition, 10° right (T-10R)*: Identical applied displacements as for *T*; however, the needle guide is tilted 10° to the right towards the right peripheral zone (PZ). The PZ is located in the back of the prostate, and close to the rectum.
- (5) *Transition, 10° left (T-10L)*: Identical applied displacements as for *T-10R*; however, the needle guide is tilted 10° to the left towards the left PZ.

Experimental case (1) is used to validate the FE model developed from MR images, while cases (2)–(5) are used to predict prostate deformations under various loadings and boundary conditions.

Table 1. Experimental cases: case T is used to validate the FE model. Prediction cases (B , A , $T-10R$ and $T-10L$) are used to predict prostate deformations under various loading and boundary conditions.

Validation	Prediction			
Transition (T)	Base (B)	Apex (A)	$T-10^\circ$ right ($T-10R$)	$T-10^\circ$ left ($T-10L$)
				

Note: The red dashed-line represents path of the needle guide during applied compressive displacements. The transition, base, apex and peripheral zone (PZ) of the prostate are shaded in grey. On the other hand, the central zone (CZ) of the prostate is shaded in blue. Transverse plane is the xz -plane, while sagittal plane is the yx -plane. Axis convention is the same as in Figure 2(d).

The effect of increasing the anatomical fidelity of the model (in terms of organs and structures surrounding the prostate) is investigated by a sensitivity study. We used the validated FE model, and the prostate deformations are studied. The organs and structures included are the urethra, puboprostatic ligament and urinary bladder. The scenarios for the sensitivity study are (Table 2):

- (1) *No urethra (NoU)*: Boundary conditions are identical as for T . The prostate is modelled without the urethra passing through it.
- (2) *Urethra and puboprostatic ligament (U-PL)*: Identical boundary conditions as for T . The prostate is attached to the pubic bone by the puboprostatic ligament.
- (3) *Urethra and urinary bladder (U-UB)*: Identical boundary conditions as for T and the urinary bladder are included in the FE model.
- (4) *Urethra, puboprostatic ligament and urinary bladder (U-PL-UB)*: Identical boundary conditions as for T . The prostate is attached to the pubic bone by the puboprostatic ligament and modelled with the urethra passing through it. The urinary bladder is also included in the FE model.

Table 2. Scenarios of the sensitivity study: anatomical fidelity of the validated FE model is investigated by including the urethra, puboprostatic ligament and urinary bladder in the model.

Nomenclature	Urethra (U)	Puboprostatic ligament (PL)	Urinary bladder (UB)
<i>NoU</i>	×	×	×
<i>U-PL</i>	✓	✓	×
<i>U-UB</i>	✓	×	✓
<i>U-PL-UB</i>	✓	✓	✓
<i>PL-UB</i>	×	✓	✓

Note: ✓ and × show the presence and absence of the organ in the model, respectively.

- (5) *Puboprostatic ligament and urinary bladder (PL-UB)*: Identical boundary conditions as for $U-PL-UB$. The prostate is modelled without the urethra passing through it.

2.2 FE model

Previous work by Misra et al. (2009) showed that with accurate modelling of prostate geometry and boundary conditions, a linear elastic FE model can be used to predict soft-tissue deformations. Thus, in our study, material property is assumed to be isotropic and linearly elastic. The constitutive equation is given by Reddy (2005)

$$\sigma = \frac{E}{1 + \mu} \epsilon + \frac{E\mu}{(1 + \mu)(1 - 2\mu)} \text{tr}(\epsilon)\mathbf{I}, \quad (1)$$

where σ and ϵ are the stress and strain tensor, respectively. In Equation (1), tr is the trace operator, \mathbf{I} is the second-order identity tensor, E is Young's modulus and μ is Poisson's ratio. Furthermore, the strain tensor is related to the FE model nodal displacements \mathbf{u} by

$$\epsilon = \frac{1}{2} \left[\nabla \mathbf{u} + (\nabla \mathbf{u})^T + (\nabla \mathbf{u})^T (\nabla \mathbf{u}) \right]. \quad (2)$$

In our study, Young's modulus is estimated using a commercially available implementation of ARFI imaging technique, or known as Virtual Touch™ Quantification, installed on a Siemens Acuson S2000 ultrasound machine (Siemens AG, Erlangen, Germany). The ARFI imaging technique provides the shear wave velocity for the defined region of interest. Young's modulus is related to shear wave velocity by Krautkramer and Krautkramer (1990)

$$E = 2(1 + \mu)v_s^2\rho, \quad (3)$$

Table 3. The Young's modulus (E) for the various structures of the FE model (item # – Figure 2(d)).

Item #	Structure	E_{ARFI}	E_{CT}
7	Perineal membrane	2.60 MPa	
8	Prostate	3.74 kPa	3.82 kPa
9	Urethra	20.0 kPa	
10	Rectal wall	24.0 kPa	
11	Surrounding gel	24.0 kPa	23.8 kPa
4	Needle guide	$E_{\text{plastic}} = 1.1 \text{ GPa}$	

Notes: E_{ARFI} is computed using Equation (3), with the shear wave velocity measured using the ultrasound-based ARFI imaging technique. E_{CT} is obtained from the compression tests using a rheometer. E_{plastic} represents the Young's Modulus of the needle guide which is made from plastic. Values of E_{ARFI} and E_{CT} are the average of three measurements. Moreover, the discrepancies noted between E_{ARFI} and E_{CT} are within the tolerance of the ARFI imaging technique reported by Palmeri et al. (2008).

where v_s is the velocity of a shear wave and ρ is the material density. In our experiment, μ is assumed to be 0.495 for a nearly incompressible prostate phantom. Moreover, according to the specification of the prostate phantom, ρ is given as the density of water. The elasticity values used in the FE model are given in Table 3.

In order to verify Young's modulus estimated using the ARFI imaging technique, compression tests were performed. The tests were done using a rheometer (Anton Paar, Gentbrugge, Belgium), and three cylindrical specimens (diameter and thickness of 25 and 24 mm, respectively) of the surrounding gel and the prostate, respectively. The surrounding gel and prostate are chosen since their elasticity values differ significantly. Initially, the specimen was carefully placed between the loading plates of the rheometer, and distance of the loading plates was adjusted such that the plates just touch the specimen. Compression was then applied at a rate of 8×10^{-3} mm/s and up to a total strain of 30%. The rheometer measures the resulting normal force and the change in the gap between the two loading plates in order to determine stress and strain, respectively. The elasticity values of the prostate and surrounding gel obtained from the compression tests are also presented in Table 3.

For the simulations, a 3D FE model is developed from MR images using a commercial software ScanIP + FE Module (Simpleware Ltd, Exeter, UK). The segmentation of MR images is done by using a combination of greyscale thresholding and the confidence-connected-region-growing techniques that are available in the ScanIP module.

Moreover, the FE mesh generated using the ScanIP + FE module consists of 10-node tetrahedral elements with element edge length of 2 mm. The FE analysis is performed using ANSYS Mechanical (ANSYS, Inc., Canonburgh, PA, USA). A mesh resolution study confirmed that the element edge length of 2 mm produces consistent results. A further reduction in the element edge length does not result in an improvement in the prediction of prostate deformation.

2.3 Contact boundary conditions

Initially, the needle guide is positioned such that the tip of the guide just touches the rectal wall of the prostate phantom. This is taken as the zero reference point. The needle guide is then displaced by 9 and 18 mm along the guide cylindrical axis (Figure 2(d)). The contact between the needle guide and the surface of the rectal wall is modelled as a frictionless contact, allowing free sliding at the contact interface. The needle guide is constrained to move only along its cylindrical axis. Moreover, in the FE model, the acrylic container is modelled with a fixed boundary condition. This is due to the fact that the acrylic container is relatively stiff, and it is secured by fixed supports during the experiments conducted in the MR imaging system.

The contact between the prostate and surrounding gel is modelled as a bonded contact. During fabrication of the prostate, the prostate and surrounding gel are made separately. The prostate is then placed within the surrounding gel prior to solidification of the gel. This allows the prostate to bond with the surrounding gel.

3. Results

This section presents the results of the experimental cases (Table 1) and the sensitivity study (Table 2).

3.1 Experimental cases

In order to analyse 3D deformation, outlines of the prostate are obtained from the FE simulations and experimental results. These outlines are taken in both transverse and sagittal planes. Figure 3 summarises the qualitative results of FE analysis and experiments for both transverse and sagittal planes. Case T is the validation case, while cases B , A , $T-10R$ and $T-10L$ are the prediction cases. It is seen that with accurate modelling of prostate geometry and boundary conditions, a linear elastic FE model can be used to predict 3D prostate deformations. An FE model of the prostate with the transverse and sagittal planes is shown in Figure 4(a). Moreover, Figure 4(b) presents outlines of the prostate for representative case T and 18 mm applied displacement, overlaid on the corresponding MR images of the prostate phantom.

Quantitatively, to calculate errors in the FE simulations, we compute the maximum absolute distance between the prostate outlines obtained from the simulations, and from the experimental results. Local error is defined as the errors noted in the transverse and sagittal planes, and the results are presented in Table 4. Global error is measured as follows (Figure 4(a)):

- (1) Errors are calculated in the parallel planes $//_T$, including the transverse plane. The value and location

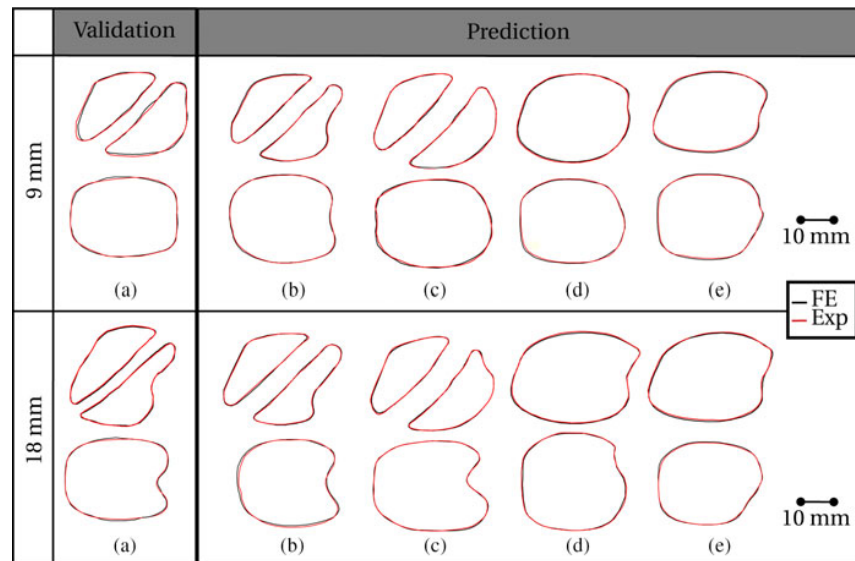


Figure 3. Outlines of the prostate obtained from the FE simulations and experimental results. Outlines are presented in transverse and sagittal planes and for experimental cases: (a) *T*, (b) *B*, (c) *A*, (d) *T-10R* and (e) *T-10L*. The transverse and sagittal planes are taken through the location where the maximum nodal displacement is noted. In all cases, applied displacements are 9 and 18 mm. Case *T* is used to validate the FE model, while cases *B*, *A*, *T-10R* and *T-10L* are used to predict prostate deformations under various loading and boundary conditions. A length scale is also included in the figure.

of the maximum error in planes $//_T$ are noted (Figure 4(a), step I).

- (2) Subsequently, a plane normal to the transverse plane (plane \perp) is taken through the location where the maximum error is noted.
- (3) In plane \perp , error is calculated at the corresponding location of the maximum error (Figure 4(a), step II). This is defined as the complement error.
- (4) Overall error based on planes $//_T$ is given by the root sum squares of the maximum and complement errors.
- (5) The same procedure (steps #1–4) is applied in the parallel planes $//_S$ (inclusive of the sagittal plane), and the overall error based on the planes $//_S$ is calculated. For planes $//_S$, plane \perp is normal to the sagittal plane.
- (6) Global error is the maximum of the two overall errors (based on planes $//_T$ and $//_S$). The results are also presented in Table 4.

The maximum local error in the validation case *T* is 0.70 mm, and it is noted in the transverse plane for 18 mm applied displacement. In the prediction cases, prostate deformations computed by the FE model result in small local errors. The maximum local error is also 0.70 mm, and it is noted in case *B* for 18 mm applied displacement (transverse plane). The global error in the validation case *T* for 9 and 18 mm applied displacement is 0.56 and 0.71 mm, respectively. In the prediction cases, the maximum global error is 0.76 mm, and it is noted in case *B* for 18 mm applied displacement.

To further highlight the importance of accurately modelling anatomical details (prostate geometry and boundary conditions) in 3D, the resultant magnitude of the predicted nodal displacements for each case is computed, and shown as contour plots in Figure 5. These plots are presented for validation and prediction cases. For both Figures 3 and 5, transverse and sagittal planes are taken through the location where the maximum nodal displacement is noted.

It is observed that, for the same magnitude of applied displacement, differences in the location of the applied displacement result in varying contour plots (Figure 5). Thus, it can be deduced that displacement fields are sensitive to geometry and boundary conditions. In cases *T*, *B* and *T-10R*, the maximum nodal displacement is noted at the area where the tip of the needle guide touches the rectal wall. For these cases, the maximum nodal displacement is 1.6 and 5.5 mm for 9 and 18 mm applied displacement, respectively.

3.2 Sensitivity study

The effects of increasing anatomical fidelity of the model are investigated by analysing FE-predicted prostate deformations. The maximum nodal displacement noted from the sensitivity study is compared with experimental case *T* (Figure 5(a)). In case *T*, only the urethra is included in the FE model. Table 5 summarises the results of the sensitivity study. Case *T* is used in this study as the basis of

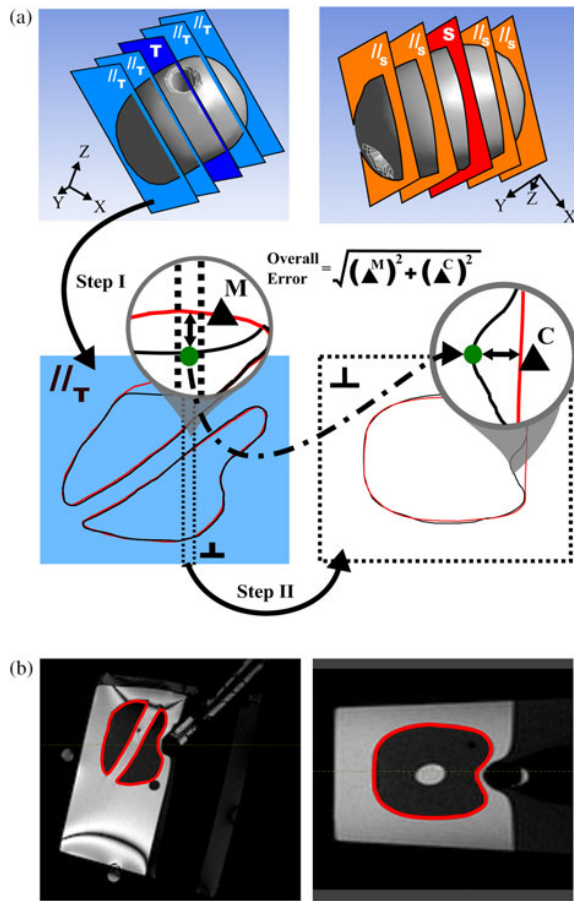


Figure 4. (a) Steps for calculating global errors. In (a), the two images on the top show an FE model of the prostate with transverse (T), sagittal (S), and parallel planes ($//_T$ and $//_S$). Planes $//_T$ and $//_S$ are parallel to the transverse and sagittal plane, respectively. The spacing between each of the planes ($//_T$ and $//_S$) is 2 mm, and the number of planes in the T and S directions is 20. \blacktriangle^M and \blacktriangle^C represent the maximum and complement error, respectively. \perp represents a plane that is normal to the transverse plane and passes through the location where \blacktriangle^M is noted (dark green dot). The same procedures (steps I and II) are also applied in the planes $//_S$. For planes $//_S$, plane \perp is normal to the sagittal plane. (b) Outlines of the FE-predicted prostate deformation overlaid on the corresponding MR images of the prostate phantom. The outlines are for representative case *T* and 18 mm applied displacement (Figure 3(a), 18 mm). The left and right images in (b) are for transverse and sagittal plane, respectively.

comparison, and its results are also included in Table 5. The scenarios of the sensitivity study are *NoU*, *U-PL*, *U-UB*, *U-PL-UB* and *PL-UB*, where *U*, *UB* and *PL* represent the urethra, urinary bladder and puboprostatic ligament, respectively (Table 2).

In comparison with case *T*, the results show that the exclusion of the urethra in the FE model (*NoU*) results in non-significant changes in prostate deformations (Table 5). Nevertheless, the inclusion of the puboprostatic ligament (*U-PL*) produces larger prostate deformations than in

case *T*. The increase in the maximum nodal displacement in scenario *U-PL* for 9 and 18 mm applied displacement is 0.13 and 0.14 mm, respectively. On the other hand, the addition of the urinary bladder (*U-UB*) results in smaller prostate deformations. The decrease in the maximum nodal displacement in scenario *U-UB* for 9 and 18 mm applied displacement is 0.01 and 0.06 mm, respectively.

Moreover, in scenario *U-PL-UB*, the effect of including both the puboprostatic ligament and urinary bladder in the FE model seems to counterbalance each other, resulting in non-significant changes in prostate deformations with respect to case *T*. However, the exclusion of the urethra (*PL-UB*) seems to perturb the balance, resulting in larger prostate deformations than in scenario *U-PL-UB*.

It should be noted that the sensitivity study does not equate a decrease or an increase in the maximum nodal displacement to a better FE model performance. The aim of this study is to investigate the effect of increasing anatomical fidelity of the FE model, and the maximum nodal displacements are used as a metric to compare the results of each scenario.

4. Discussion

Standard medical imaging modalities such as ultrasound and MR images are routinely used for the diagnosis of prostate cancer. Our study illustrates that a combination of ultrasound-based ARFI imaging technique, MR images and FE analysis can be used to develop a patient-specific anatomically accurate biomechanical prostate model. Our study also shows that the estimation of the linear elastic soft-tissue properties for small strain can be done *in vivo* using the ARFI imaging technique.

Furthermore, the results of our study confirm that 3D prostate deformation is predominantly dependent on accurate modelling of anatomical details (prostate geometry and boundary conditions). Thus, a linear elastic FE model can be used to predict prostate deformations. This observation is consistent with the previous study by Misra et al. (2009) in 2D. In our study, the maximum local and global errors between the FE-predicted simulations and experimental results are 0.70 and 0.76 mm, respectively. The errors can be attributed to the segmentation error and noise in the MR images which are related to the resolution of 3D MR images (1 mm \times 1 mm \times 1 mm).

Moreover, a sensitivity study is conducted to investigate the effect of increasing fidelity (in terms of organs and structures surrounding the prostate) of the FE model. Organs and structures considered are the urethra, puboprostatic ligament and urinary bladder. The results of the sensitivity study indicate that the exclusion of the urethra in the FE model does not influence the prostate deformations significantly. On the other hand, the inclusion of the puboprostatic ligament and urinary bladder increases and decreases prostate deformations, respectively.

Table 4. Errors between the outlines of the prostate obtained from FE simulations (Sim) and experimental results (Exp).

Sim versus Exp		Validation T (mm)	Prediction			
			B (mm)	A (mm)	$T-10R$ (mm)	$T-10L$ (mm)
9 mm	Transverse	0.50	0.50	0.41	0.52	0.51
	Sagittal	0.39	0.49	0.39	0.50	0.49
	Global	0.56	0.60	0.46	0.61	0.57
18 mm	Transverse	0.70	0.70	0.48	0.61	0.60
	Sagittal	0.28	0.49	0.49	0.39	0.48
	Global	0.71	0.76	0.59	0.66	0.67

Note: Transverse and sagittal are the local error noted in transverse and sagittal plane, respectively. Global error is the maximum of the two overall errors that are based on planes // r and // s . Errors are presented for 9 and 18 mm applied displacements.

Nevertheless, for all scenarios, the changes in the prostate deformations caused by increasing fidelity of the FE model are small. The absolute values of the changes (based on the maximum nodal displacement) for all scenarios are less than 0.15 mm. This phenomenon might be attributed to the fact that the prostate (item #8, Figure 2(d)) is completely surrounded by stiff gel (item #11, Figure 2(d)). On the other hand, in the human body, the prostate is surrounded by relatively soft adipose tissue. Furthermore, organs and structures might be loosely packed in the pelvic cavity. Thus, prostate deformations in the body might be more significant in comparison to the phantom. Subsequently, during biopsy, the presence of the

urethra, puboprostatic ligament and urinary bladder might have a greater effect on prostate deformations.

For future work, we will extend the results of our study to be applicable to a surgical simulation system. A simulator that can predict soft-tissue deformations in real time can also be used as a control input for a robotic system (Fichtinger et al. 2008). Two major challenges need to be overcome in order to use a biomechanical model, based on FE analysis, for a surgical simulation system. First, the model needs to incorporate soft-tissue properties based on *in vivo* data. Second, the FE analysis has to run in real time, which can be computationally challenging.

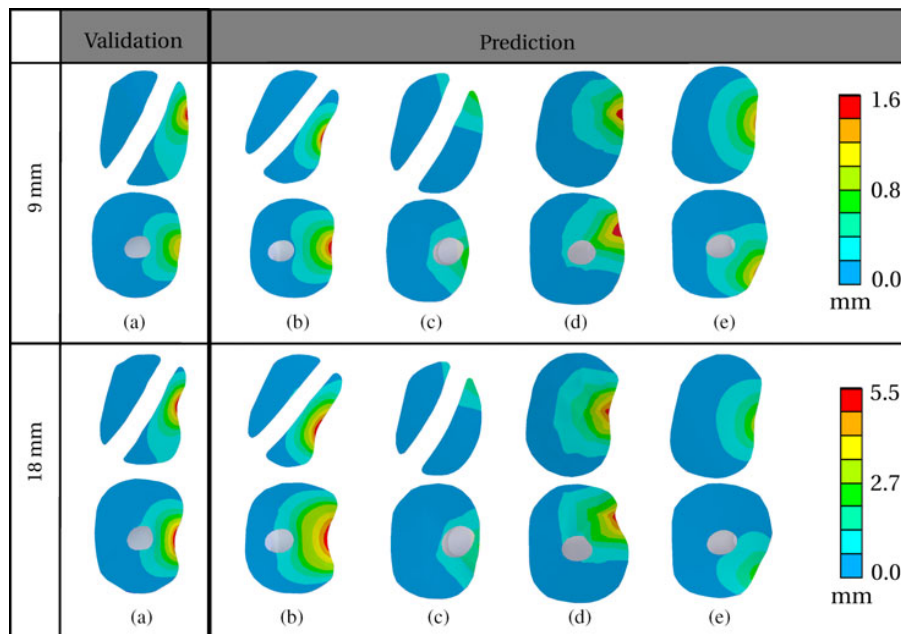


Figure 5. Contour plots of the resultant magnitude of the predicted nodal displacements. Plots are presented in transverse and sagittal planes, and for experimental cases: (a) T , (b) B , (c) A , (d) $T-10R$ and (e) $T-10L$. Case T is also used as a basis of comparison in the sensitivity study. The applied displacements for all cases are 9 and 18 mm. Transverse and sagittal planes are taken through the location where the maximum nodal displacement is noted. The first and third row images are for the transverse plane, while the second and fourth row images are for the sagittal plane. The urethra passes through the prostate, and is the grey region in the sagittal plane images.

Table 5. Maximum nodal displacements noted in case *T*, and in the scenarios of the sensitivity study.

FE	Disp (mm)	<i>T</i> (mm)	<i>NoU</i> (mm)	<i>U-PL</i> (mm)	<i>U-UB</i> (mm)	<i>U-PL-UB</i> (mm)	<i>PL-UB</i> (mm)
Total	9	1.60	1.61	1.73	1.59	1.61	1.63
	18	5.49	5.52	5.63	5.43	5.53	5.61
Δ	9		+0.01	+0.13	-0.01	+0.01	+0.03
	18		+0.03	+0.14	-0.06	+0.04	+0.12

Note: Case *T* is used as the basis of comparison. Disp represents an applied displacement. Δ represents the change in the maximum nodal displacement with respect to case *T*, and (-) and (+) represent a negative and positive change, respectively.

The use of the ultrasound-based ARFI imaging technique allows *in vivo* estimation of soft-tissue properties. However, the accuracy of the ultrasound-based measurements depends on factors such as physiological motion and the penetration of acoustic energy through the skin and fat (Dick et al. 2002). Nevertheless, previous study by Palmeri et al. (2008) showed that the application of linear motion filter and goodness of fit metrics decreased the influences of these factors. In our study, the implementation of eSie Touch Imaging Technology on the Siemens Acuson S2000 ultrasound machine allows the *in vivo* quantification of elasticity imaging in real time. Using this technology, the ultrasound machine provides a quality factor that indicates measurement errors due to axial, lateral and global motion artifacts. Subsequently, this factor is used to optimise and minimise the acquisition techniques and measurement errors, respectively (Siemens Medical Solutions, USA, Inc. 2010).

As part of future work, we also plan to confirm the results of our current study by using *in vivo* data and MR-compatible markers. The use of markers will allow the maximum prostate deformations to be obtained directly from MR images. Moreover, changes in the positions of the markers will be correlated with nodal displacements in the FE model at the locations corresponding to the markers. With regard to the computational limitation of an FE analysis, one method to circumvent this restriction is to use statistical modelling, based on training samples in which soft-tissue deformations are known (Davatzikos et al. 2001; Pezzementi et al. 2008). We will investigate the use of machine learning techniques such as neural network for accurately predicting prostate deformations. A priori biomechanical knowledge can be used as an additional input to the network in order to improve the accuracy of the predictions (Cootes and Taylor 1995; Andresen et al. 2000; Davatzikos et al. 2001).

In conclusion, in this study, we illustrate that a combination of standard medical imaging modalities can be used to estimate soft-tissue properties *in vivo*, and to develop a 3D FE model to predict prostate deformations. Our study also confirms that by accurately modelling prostate geometry and boundary conditions, a linear elastic FE model can predict prostate deformations under varying

loading conditions. Such a model can be used to aid physicians during pre-operative planning for a wide range of minimally invasive surgical interventions.

Acknowledgements

This study was supported by funds from the Dutch Ministry of Economic Affairs and the Province of Overijssel, within the Pieken in de Delta (PIDON) Initiative, Project MIRIAM (*Minimally Invasive Robotics In An MRI environment*).

References

- Alterovitz R, Goldberg K, Pouliot J, Hsu IC, Kim Y, Noworolski SM, Kurhanewicz J. 2006. Registration of MR prostate images with biomechanical modeling and nonlinear parameter estimation. *Med Phys.* 33(2):446–454.
- Anastasiadis AG, Lichy MP, Nagele U, Kuczyk MA, Merseburger AS, Hennenlotter J, Corvin S, Sievert KD, Claussen CD, Senz A, Schiemmer, HP. 2006. MRI-guided biopsy of the prostate increases diagnostic performance in men with elevated or increasing PSA levels after previous negative TRUS biopsies. *Eur Urol.* 50(4):738–748.
- Andresen PR, Bookstein FL, Couradsen K, Ersboll BK, Marsh JL, Kreiborg S. 2000. Surface-bounded growth modeling applied to human mandibles. *IEEE Trans Med Imaging.* 19(11):1053–1063.
- Benninghoff. 1993. *Makroskopische anatomie, embryologie und histologie des menschen*. 1st ed. Munich, Germany: Urban und Schwarzenberg.
- Cootes T, Taylor CJ. 1995. Combining point distribution models with shape models based on finite element analysis. *Image Vision Comput.* 13(5):403–409.
- Crouch JR, Pizer SM, Chaney EL, Hu YC, Mageras GS, Zaider M. 2007. Automated finite-element analysis for deformable registration of prostate images. *IEEE Trans Med Imaging.* 26(10):1379–1390.
- Davatzikos C, Shen D, Mohamed A, Kyriacou SK. 2001. A framework for predictive modeling of anatomical deformations. *IEEE Trans Med Imaging.* 20(8):836–843.
- Dick EA, Patel K, Owens CM, de Bruyn R. 2002. Spinal ultrasound in infants. *Br J Radiol.* 75(892):384–392.
- Fichtinger G, Fiene JP, Kennedy CW, Kronreif G, Iordachita I, Song DY, Burdette EC, Kazanzides P. 2008. Robotic assistance for ultrasound-guided prostate brachytherapy. *Med Image Anal.* 12(5):535–545.
- Goertz RS, Zopf Y, Jugl V, Heide R, Janson C, Strobel D, Bernatik T, Haendl T. 2010. Measurement of liver elasticity with acoustic radiation force impulse (ARFI) technology: an

- alternative noninvasive method for staging liver fibrosis in viral hepatitis. *Ultraschall Med.* 31(2):151–155.
- Hu YP, Morgan D, Hashin A, Pendsé D, Sahu M, Allen C, Emberton M, Hawkes D, Barratt D. 2008. Modelling prostate gland motion for image-guided interventions. In: *Proceedings of the 4th International Symposium of Biomedical Simulation (ISBMS)*. July. London, UK. p. 79–88.
- Karnik VV, Fenster A, Bax J, Cool DW, Gardi L, Gyacskov I, Romagnoli C, Ward A. 2010. Assessment of image registration accuracy in three-dimensional transrectal ultrasound guided prostate biopsy. *Med Phys.* 37(2):802–813.
- Krautkramer J, Krautkramer H. 1990. *Ultrasonic testing of materials*. 4th ed. New York, USA: Springer-Verlag.
- Kundra V, Silverman PM, Matin SF, Choi H. 2007. Imaging in oncology from the University of Texas M.D. Anderson Cancer Center: diagnosis, staging, and surveillance of prostate cancer. *Am J Roentgenol.* 189(4):830–844.
- Misra S, Macura KJ, Ramesh KT, Okamura AM. 2009. The importance of organ geometry and boundary constraints for planning of medical interventions. *Med Phys.* 31(2):195–206.
- Misra S, Ramesh KT, Okamura AM. 2008. Modeling of tool-tissue interactions for computer-based surgical simulation: a literature review. *Presence Teleoperator Virtual Environ.* 17(5):463–491.
- Mohamed A, Davatzikos C, Taylor R. 2002. A combined statistical and biomechanical model for estimation of intra-operative prostate deformation. In: *Proceedings of the 5th International Conference on Medical Image Computing and Computer-Assisted Intervention (MICCAI)*. London, UK. p. 452–460.
- Nichol AM, Brock KK, Lockwood GA, Moseley DJ, Rosewall T, Warde PR, Catton CN, Jaffray AD. 2007. A magnetic resonance imaging study of prostate deformation relative to implanted gold fiducial markers. *Int J Radiat Oncol Biol Phys.* 67(1):48–56.
- Op den Buijs J, Hansen HH, Lopata RG, de Korte CL, Misra S. 2011. Predicting target displacements using ultrasound elastography and finite element modeling. *IEEE Trans Biomed Eng.* 58(11):3143–3155.
- Ophir J, Céspedes I, Ponnekanti H, Yazdi Y, Li X. 1991. Elastography: a quantitative method for imaging the elasticity of biological tissues. *Ultrasound Imaging.* 13(2):111–134.
- Ottensmeyer MP, Kerdok AE, Howe RD, Dawson SL. 2007. The effects of testing environment on the viscoelastic properties of soft tissues. *Perfusion.* 24(3):219–238.
- Palmeri ML, Wang MH, Dahl JJ, Frinkley KD, Nightingale KR. 2008. Quantifying hepatic shear modulus in vivo using acoustic radiation force. *Ultrasound Med Biol.* 34(4):546–558.
- Pezzementi Z, Ursu D, Misra S, Okamura AM. 2008. Modeling realistic tool-tissue interactions with haptic feedback: a learning-based method. In: *Proceedings of the 16th Symposium on Haptic Interfaces for Virtual Environment and Teleoperator Systems (IEEE)*. March. Reno, USA. p. 209–215.
- Reddy JN. 2005. *An introduction to the finite element method*. 3rd ed. New York, USA: The McGraw-Hill Companies.
- Shahrokh FS, Claus GR. 2008. Using biopsy to detect prostate cancer. *Rev Urol.* 10(4):262–280.
- Siemens Medical Solutions, USA, Inc. 2010. *ACUSON S2000 diagnostic ultrasound system: instructions for use*. 2nd ed. Mountain View, USA: Siemens Medical Solutions, CA, USA, Inc.
- Wust P, von Borczyskowski DW, Henkel T, Rosner C, Graf R, Tilly W, Budach V, Felix R, Kahmann F. 2004. Clinical and physical determinants for toxicity of 125-I seed prostate brachytherapy. *Radiother Oncol.* 73(1):39–48.